SAND2005-7970C

Imaging of dissipative structures in the near field of a turbulent non-premixed jet flame

Sebastian A. Kaiser and Jonathan H. Frank

Combustion Research Facility
Sandia National Laboratories
Livermore, CA 94551, USA

Abstract

Two-dimensional laser Rayleigh measurements of thermal gradient structures are performed in a turbulent non-premixed jet flame. The measurements focus on the near field (10 nozzle diameters downstream of the jet exit) where traditional scaling laws from the self-similar mixing-dominated far field of jet flames and non-reacting jets are not necessarily applicable. The optical performance of the high-resolution imaging system is characterized. The square of the temperature gradient field is analyzed by calculating the power spectral density (PSD) and by direct measurement of the thicknesses of the layer-like structures that are seen in the images. Fully resolved spectra extending over three orders of magnitude in PSD are obtained using a new noise cancellation technique. Some spatial filtering (smoothing) is necessary to reliably measure the layer-normal structure widths in the images. The probability density function (PDF) of the layer widths is found to be approximately log-normal. The PDFs of the 20-percent-full-width layer thicknesses had peak values at 216 micrometer and 368 micrometer for r/d = 0 and r/d = 1, respectively. The peak of the layer-thickness probability density function (PDF) occurs at a length scale where the PSD is at approximately 0.5 percent of its maximum in both the low-temperature centerline region and the region near the maximum mean temperature.

1 Introduction

In turbulent flows, dissipation is a fundamental quantity governing the rate of molecular mixing. It therefore is prominent in theoretical analysis, models, and numerical simulations of turbulent flames. The scalar dissipation rate $\chi=2D(\nabla\xi\bullet\nabla\xi)$, where D is the mass diffusion coefficient and ξ is the mixture fraction, can be thought of as an inverse time scale that determines to what degree the local flame chemistry deviates from equilibrium. Dissipation occurs at the smallest scales of turbulence, which have to be either discretely resolved or correctly modeled in numerical simulations.

Precisely because the smallest flow scales need to be resolved, reliable dissipation measurements are difficult even in non-reacting flows. Probe-based time series measurements in the far field of non-reacting jets have established scaling relations that allow estimation of the Kolmogorov scale η. In the far field of jet flames, the flow is mixing-dominated, and it is plausible to use relations established for non-reacting flows to obtain microscale estimates. However, the near field ($x/d<30$) of jet flames is not self-similar and shows strong mean gradients of velocity and scalar fields [1]. The applicability of traditional scaling relations in the near field is therefore questionable.

The situation is compounded by the severe tradeoff between spatial resolution and noise-induced bias in dissipation measurements. For example, in an imaging measurement of the mean dissipation the additive mean noise bias

due to evaluation of $(\nabla\xi \bullet \nabla\xi)$ scales as the negative-fourth power of the resolution [2, 3]. A measurement may be nominally "resolved" but meaningless due to this bias. On the other hand, the lack of sufficient resolution will "wash out" the measured gradients and lead to an under-prediction of the dissipation.

Mixture fraction is the most fundamental scalar in non-premixed combustion. However, the determination of mixture fraction requires multiple simultaneous measurements of species concentrations and temperature. Hence only line measurements with modest spatial resolution [4, 5] and imaging experiments relying on assumptions about the underlying state-space of the flow [6 - 9] have been possible. Measurements of the instantaneous temperature field, via laser Rayleigh scattering, can be accomplished with much higher resolution and signal/noise ratio (SNR). In typical laboratory jet flames with low probability of extinction the thermal structure is strongly correlated with the mixture-fraction structure, as can be seen in scatter plots of T vs. ξ [10, 11]. Around the stoichiometric value of ξ, the temperature gradient goes to zero, yielding two separate structures in $(\nabla T \bullet \nabla T)$. In general, one would therefore expect the typical structure in the thermal gradient to be comparable to or smaller than the underlying structure in the conserved scalar gradient $\nabla\xi$. While the general validity and limits of such correlations will be the subject of future detailed investigation, for example using results of direct numerical simulations (DNS) that include extinction and re-ignition phenomena [12], we will simply restrict the scope this paper to the thermal structure. Regardless of their connection to the conserved scalar, well-understood imaging data should be ideally suited for comparison with spatially resolved numerical models such as Large Eddy Simulations (LES).

Laser Rayleigh scattering is a widely used technique for temperature measurements in flames [1,6,9,11,13,14]. Everest et al. [14] applied planar Rayleigh imaging to a turbulent jet flame with constant Rayleigh cross-section, calculated the instantaneous thermal dissipation fields, and derived some statistical measures. Dissipation was found to be organized in sheet-like (or layer-like) structures, as it is in non-reacting flows. While this study provided valuable insight into the structure of the flame, extensive implicit and explicit filtering of the data was necessary to suppress noise, rendering the actual resolution inadequate for quantitative measurements of the smallest scales for all but the lowest Reynolds numbers investigated. Bergmann et al. [1] mapped large regions of a flame that is nearly identical to the one investigated here by Rayleigh imaging, presented some estimates of maximum thermal dissipation for one particular location, and documented the response of the thermal structure to variations in the jet Reynolds number. Wang et al. [15] studied the far field of the same jet flame by a time-series of Rayleigh point measurements and found that on the jet centerline the dissipative scaling and the probability density function (PDF) of thermal dissipation were similar to that of non-reacting jets. The fine-scale dissipative structures of non-reacting, gaseous flows have been studied in more detail. For example, Buch and Dahm [16] measured the dissipative scales in the far field of a round propane jet with two-dimensional Rayleigh imaging and determined the probability density function (PDF) of the dissipation layer thickness. Most recently, Su and Clemens [17, 18] used combined Rayleigh scattering and Planar Laser-Induced Fluorescence (PLIF) in two closely spaced planes to obtain the full three-dimensional scalar gradient vector with high resolution.

Thermal dissipation, $\chi_T = 2\alpha(\nabla T' \bullet \nabla T')$, depends on both the gradient of the temperature fluctuation and the local thermal diffusivity α. The

thermal diffusivity approximately scales with temperature as $\alpha \propto T^{1.72}$ [19] and varies by a factor of ~27 over the temperature range in the flame considered here. As a result, measurements of χ_T at high temperatures are significantly more sensitive to noise than are measurements of the gradient-squared term, $|\nabla T'|^2 \equiv (\nabla T' \bullet \nabla T')$ [19]. In the present study, we focus on the $|\nabla T'|^2$ term because it contains significant structural detail of the dissipation field and is less sensitive to noise than χ_T. We measure temperature in the near field of a turbulent jet flame with high resolution and low noise in order to analyze the small-scale structures of turbulence in a reacting flow.

2 Experiment

The experiment was performed in the Advanced Imaging Laboratory at Sandia National Laboratories. The non-premixed turbulent jet flame considered here corresponds to "Flame DLR-A" from the set of target flames in the TNF Workshop [20]. The fuel was a mixture of 22.1% CH_4, 33.2% H_2, and 44.7% N_2 (by volume) with the air of the coflow as the oxidizer. The stoichiometric mixture fraction ξ_{st} is 0.167. This combination of fuel and oxidizer yields a Rayleigh cross-section that is constant within ±3% throughout the flame [1], therefore allowing for direct temperature measurements from Rayleigh scattering. The fuel jet issued from a tube with a diameter of d = 8.0 mm at an exit Reynolds number of Re_d = 15,200 into the filtered air of the coflow. The mean coflow velocity was 1.5 m/s. The reproducibility of the DLR-A Flame was verified by comparing our imaging measurements of the radial profiles of the mean and root-mean-square of the temperature with the point measurements in the TNF data base [20].

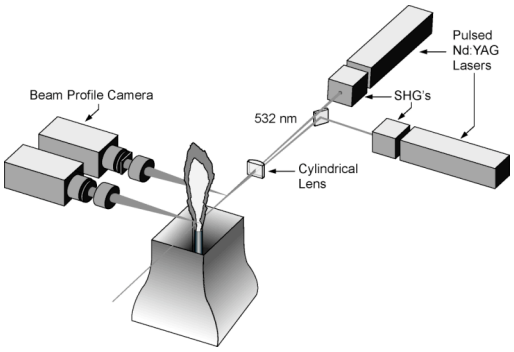

Fig. 1: High-resolution Rayleigh experiment.

2.1 Experimental Arrangement

The experimental arrangement is shown in Fig. 1. The beams of two frequency-doubled Nd:YAG lasers were combined by vertically "stacking" the beams far away (≈ 10 m) from the test section. Combined pulse energies were approximately 1.8 J at 532 nm. The laser sheet was formed by a single cylindrical lens with a focal length FL of 500 mm. The horizontal overlap and beam-waist profiles were recorded on an unintensified CCD camera (not shown in Fig. 1) coupled with a mirror that was positioned above the test section and to one side of the flame.

Rayleigh scattering from the probe volume was imaged onto an unintensified interline-transfer camera (SensiCam QE, PCO/Cooke) by the combination of a medium-format lens (Contax, FL = 80 mm, f/2), an AR-coated convex-concave singlet (FL = -400 mm), and a "35-mm" lens (Canon, FL = 50 mm, f/1.2). In this "sandwiched front-to-front" arrangement both camera lenses each were operating near their optimum performance at infinite conjugate ratio, while the addition of the negative lens allowed for a somewhat larger distance between the flame and the medium-format lens. In this monochromatic imaging application, the aberrations introduced by the singlet lens were minor. The short gating time of the camera (2 μs) suppressed flame luminosity.

A similar arrangement of an interline-transfer camera (SensiCam,

PCO/Cooke) and front-to-front coupled photographic lenses (Canon, FL = 100 mm, operating at f/4 + singlet FL = -300 mm + Nikon 58 mm, f/1.2) imaged Rayleigh scattering from air in the coflow adjacent to the probe volume to account for shot-to-shot variation in the sheet's vertical intensity profile.

2.2 Processing and Resolution

Data reduction consisted of corrections for average throughput of the imaging system as well as shot-to-shot beam-profile corrections using the frames from the beam-profiling camera. Background signal from elastic scattering was negligible. However, the Rayleigh images in flames exhibited a small amount of luminous background due to the limited extinction ratio of interline-transfer CCD chip. This effect was accounted for by subtracting an average luminosity image at the respective measurement positions in the flame. The temperature field was determined from the corrected Rayleigh signal, which is directly proportional to the gas number density. The Rayleigh scattering from room temperature air was used as a reference signal.

Rayleigh scattering from the probe volume was recorded at the full resolution of the camera with a projected pixel area of 10.4 x 10.4 μm^2. For the results presented below, the images were binned 2 x 2 (20.7 x 20.7 μm^2) in the data reduction process. At this resolution, the line spread function (LSF) of the imaging system was measured using a scanning-edge technique [21 and references therein] to have a full width at half maximum of 24 μm in the center of the image, equivalent to a standard deviation σ_{LSF} of 10.2 μm. Off-axis performance was not measured but is expected to be only slightly worse because of the small detector size (about 10 x 7.5 mm^2) compared to the much larger area usually covered by photographic lenses. Wang and Clemens [21] numerically analyzed the imaging of a scalar with an error-function profile by an optical system having a Gaussian LSF. They demonstrated that in order to keep relative errors in the measured dissipation structure thickness λ_D (full-width at 20% maximum) below 10%, σ_{LSF} needed to be smaller than λ_D by a factor of 6.1. For the present Rayleigh imaging system, this would mean that the 20%-width of structures wider than 62 μm could be determined within 10% relative error.

This uncertainty analysis omits several effects, including out-of-plane spatial averaging due to the finite laser sheet thickness, the influence of noise in the scalar measurement, and the resolution degradation due to noise-suppressing filters. The latter two issues will be examined in detail below. The average $1/e^2$ full width laser sheet thickness, which was determined by fitting a Gaussian function to the measured intensity profile, was 150 μm or equivalently, the standard deviation σ_{sheet} of the profile was 38 μm. As a result, the resolution in the out-of-plane dimension was approximately a factor of 3.7 coarser than the in-plane resolution. However, preliminary analysis of Rayleigh images taken with different beam thicknesses indicates that the effect of out-of-plane averaging on the gradients calculated by in-plane differentiation is very minor for the measurements presented here. In the analysis that follows, we neglect the influence of the finite sheet thickness.

3 Results and Discussion

Rayleigh imaging measurements were performed at three downstream positions: x/d = 5, 10, and 20. At each measurement station, a set of 600 images were acquired. In this paper, we will use images from two radial positions at x/d = 10 to investigate the scales of the dissipative structures. At this downstream location, half of the flame width could be measured by imaging two adjacent regions.

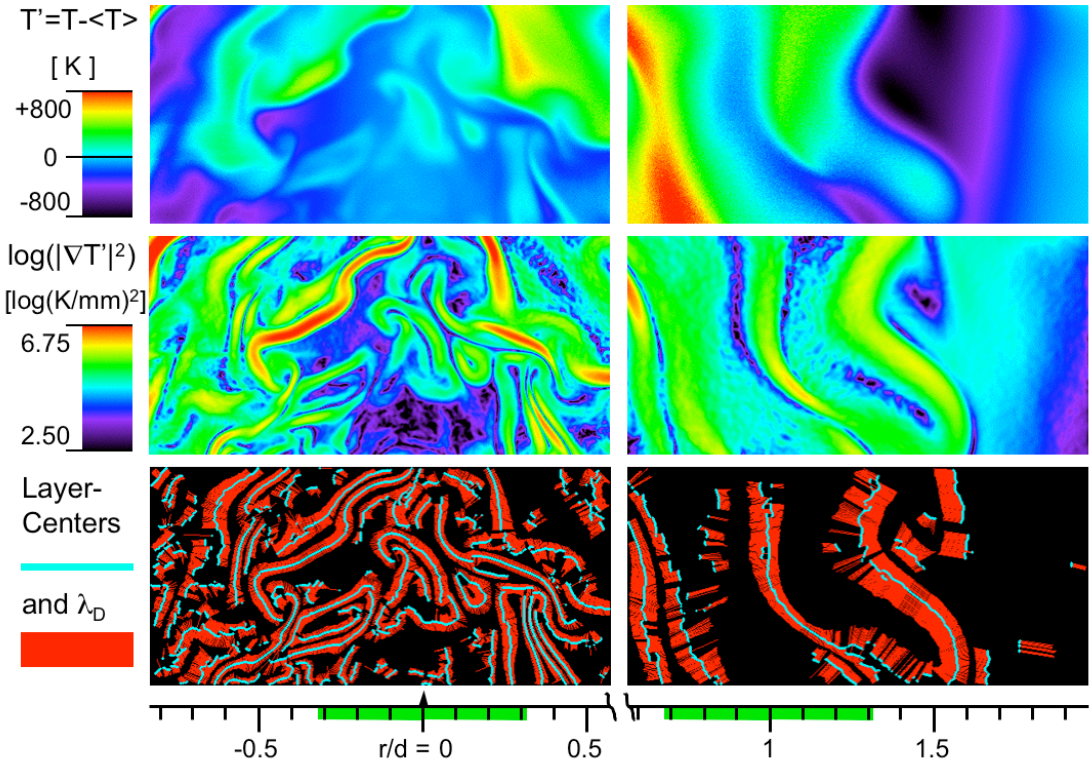

Fig. 2: Sample images of temperature fluctuations, gradient-square on a logarithmic color scale (after smoothing of T'), and layer-centers with the traces out to the 20%-width. The two image sets covering the flame at x/d = 10 were cropped to avoid overlap. Indicated in green on the ruler are the extent and positions of the sub-regions at r/d = 0 and r/d = 1 used for analysis. Axial position: x/d = 10 (d = 8mm).

Fig. 2 shows false-color images of instantaneous measurements of the temperature fluctuation, T′, and the logarithm of $|\nabla T'|^2$ at two adjacent radial locations. The measurement at each radial location was acquired separately. The layered structures in the $|\nabla T'|^2$ image are readily apparent, and a preferred orientation of the layers is induced by flow shear, especially between r/d = 0.25 and 0.75. Further towards the lean side, the flow is dominated by structures that are larger and less convoluted, which is indicative of flow laminarization due to the flame heat release. At approximately r/d = 0.7, there is a vertically elongated region of very high temperature (row 1) with a corresponding doubly-peaked structure in the $|\nabla T'|^2$ image (row 2). These double structures are expected near the stoichiometric contour where ∇T vanishes. The far right (lean) side of the imaged region is marked by the rather abrupt transition to the featureless cold coflow.

For quantitative comparisons, it is necessary to extract reliable and meaningful statistics from the full set of images. In the following sections, we consider the power density spectra of $|\nabla T'|^2$ and direct measurements of the $|\nabla T'|^2$ layer thicknesses. A visualization of the identified layer centerlines and the measured widths for the two sample shots is shown in the third row of Fig. 2.

3.1 Noise Reduction Methods

3.1.1 Noise Suppression in Power Density Spectra

In evaluating the power density spectra of $|\nabla T'|^2$, we used an interlacing technique to significantly reduce the noise

floor. Fig. 3a shows the power spectral density for the radial component of the temperature gradient, $PSD_r = |FFT_r(\nabla T')|^2$, where FFT_r indicates the forward Fast Fourier Transform in the radial direction. The spectrum is computed from 600 shots using a 20.7-μm pixel spacing in two regions of 256 x 256 pixels (5.3 x 5.3 mm^2) each, centered at r/d = 0 and r/d = 1. The PSD evaluated without interlacing exhibits a monotonic decay with increasing spatial frequency for frequencies less than 4.2 mm^{-1}. For larger spatial frequencies, noise becomes dominant, and the PSD increases. The resulting spectrum has a limited dynamic range of approximately 50. In the interlacing approach, each temperature image is separated into two fields by sampling alternate rows of pixels. To the extent that the noise in neighboring pixels is uncorrelated, the noise contribution to the mean spectrum cancels. The resulting interlaced power spectral density is given by $PSD_r^{IL} = \left|FFT_r\left(\nabla T_1'\right) FFT_r^*\left(\nabla T_2'\right)\right|$, where $\nabla T_i'$ is the gradient of the temperature fluctuation from the i^{th} field, and FFT_r^* indicates the complex conjugate of the Fast Fourier Transform. In Fig. 3a, the PSD with interlacing shows a significant reduction of the noise and indicates that the interlaced spectrum is resolved over three orders of magnitude. Noise becomes significant at frequencies greater than 5.7 mm^{-1}. Similarly to a correction technique demonstrated by Wang *et al*. [19], interlacing exploits the spatial redundancy of the data, assuming that the relevant scales are over-resolved. It can also be used to compute ensemble averages and conditional averages from imaging data.

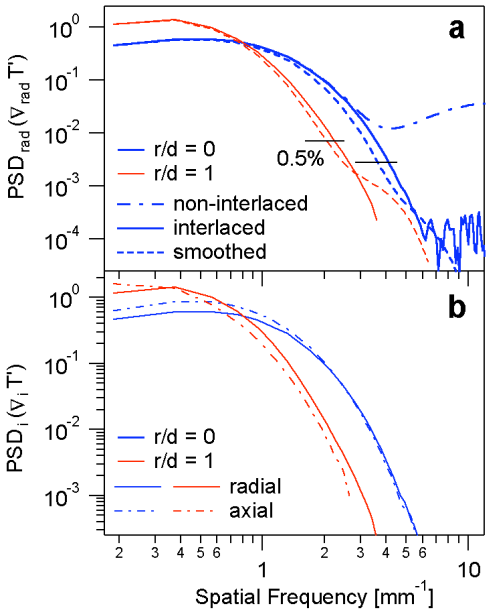

Fig. 3: One-dimensional power spectra of the temperature fluctuation gradient. All spectra normalized by the corresponding 1D mean gradient-square $\langle|\nabla T'|^2\rangle$ [24]. (a) Radial spectra calculated without interlacing, with interlacing, and with smoothing (non-interlaced, σ=2 pixels for r/d=0 and σ= 3 pixels for r/d=1). The 0.5%-of-maximum levels are indicated for each probe position. (b) Axial and radial interlaced spectra for both probe positions.

3.1.2 Single-Shot Noise Suppression

The interlacing technique is extremely useful for accurately measuring highly resolved power spectra that are averaged over many images. However, the determination of dissipation structure thicknesses requires a scheme for reducing noise on a single-shot basis. Ideally, we would filter the individual images with a kernel that has minimal impact on the power spectrum and reduces the noise enough to evaluate the thickness of dissipative structures. In this study, we implement a rather traditional filtering method using a single smoothing kernel for the entire image. We have chosen different smoothing kernels for each of the regions of interest. For the image regions centered at r/d = 0 and 1, we used Gaussian smoothing kernels with σ = 41.4 μm (2 pixels) and 62.1 μm (3 pixels),

respectively. The smaller kernel was used in the low temperature region where the spatial scales were smaller and the average noise level was lower. The relative scales in the two regions are evident from the unsmoothed temperature images and power spectra. The effect of this smoothing on the radial power spectrum is shown in Fig. 3a. The smoothing attenuates a portion of the spectrum, but the ability to fully resolve the spectrum using interlacing allows us to estimate the effects of the smoothing on the results. Less extensive filtering may be possible with alternative filtering methods such as adaptive smoothing and further optimization of the algorithm for determining structure thicknesses.

3.2 Power Spectra of Dissipative Structures

Spectral analysis is a powerful tool for the investigation of the dissipative length scales. The interlacing technique was used to compare highly resolved power density spectra of dissipative structures at two radial locations in the jet flame. The imaging data provided measurements of spectra for both the radial and axial temperature gradients. For the spectra of axial gradients, interlacing was performed by sampling alternate columns of the temperature-fluctuation images and evaluating the gradient along each column. Fig. 3b shows axial and radial spectra for r/d = 0 and 1 averaged over 600 shots. The spectra capture some features that can be seen in the sample images of Fig. 2: While the shape of the spectra is similar at the two radial locations, the jet centerline spectrum extends to significantly higher spatial frequencies than the spectrum for r/d = 1. The higher spatial frequencies on the jet centerline arise from the smaller structures associated with turbulent mixing in the low-temperature region of the jet. At high frequencies, the axial and radial spectra from r/d = 0 are nearly identical, while those from r/d = 1 show a lower axial PSD. For both locations, the axial PSD is larger than the radial PSD at the lowest frequencies. This can be reconciled with the relatively isotropically oriented small structures in the cold flow near the centerline, and the more vertically oriented structures in the laminarized hot portion of the flow. The progression of the spectrum from the jet centerline to the higher-temperature location at r/d=1 is characteristic of the near field of a jet flame and is distinctly different from the self-similar behavior in the far field of reacting and non-reacting jets.

3.3 Direct measurement of the dissipative layer thickness

Imaging measurements provide intuitive and "direct" insight into the structure of turbulent flow. A characteristic width of the dissipative structures can be directly determined from the instantaneous images of $|\nabla T'|^2$. For consistency with similar studies in non-reacting flows [16–18, 22], we measured the full width of the layer-like structures at 20% of the local maximum of $|\nabla T'|^2$. This layer width, λ_D, was determined by a procedure similar to that of Su and Clemens [18, p. 17] and consisted of three basic steps:

- Find the centerlines of the $|\nabla T'|^2$-layers
- Discard centerlines shorter than a certain minimum length
- Measure layer thickness perpendicular to the centerline

The 20%-half-width was measured separately on each side of the layers, and the half-width was doubled to yield the full 20%-width, λ_D. Figure 2 shows a sample of the half-width layer thicknesses (red lines) that were determined along each of the layer centerlines (blue lines). In some cases, the layer half-width was not found because the perpendicular profile of $|\nabla T'|^2$ did not monotonically decay to the 20% point.

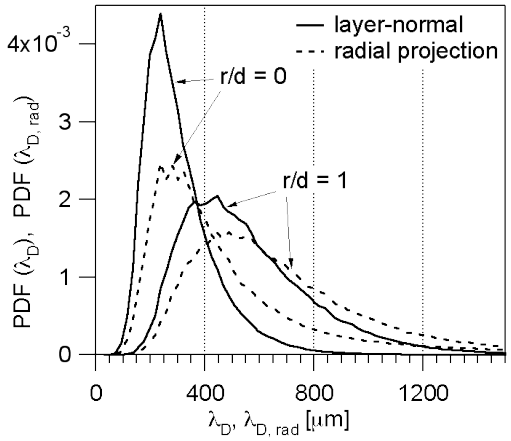

Fig. 4: PDFs of the layer widths at r/d = 0 and r/d = 1 from the 2D-layer-normal measurement (solid) and the 1D-projections onto the radial dimension based on the local gradient angle (dashed).

The PDFs of λ_D for the two probe locations are shown in Fig. 4. The peaks of the PDFs, $\lambda_{D,peak}$, are at approximately 240 μm on the jet-centerline (r/d = 0) and 400 μm for the high-temperature zone (r/d = 1). An error estimate based on the analysis of Wang and Clemens [21] indicates that Gaussian smoothing with $\sigma = 2$ pixels ($\sigma = 3$ pixels) introduces an error of 11% (9%) for a measured layer thickness of 240 μm (400 μm). The error increases for λ_D less than $\lambda_{D,peak}$, and decreases for λ_D greater than $\lambda_{D,peak}$.

At both probe positions, the PDFs have long tails that extend towards large λ_D. These tails may partially result from the two-dimensional measurement of a three-dimensional structure. In non-reacting jets, Buch and Dahm [16] find that correction of this 2D-bias with a deconvolution technique [23] (assuming flow isotropy) removes these tails entirely. However, Su and Clemens [18], report an asymmetric PDF from three-dimensional measurements of the scalar gradient. It should be noted that higher noise levels in the scalar images lead to a negative bias for large layer thicknesses and thereby reduce the tail of the PDF. This bias arises because broad $|\nabla T'|^2$-layers have a smaller gradient, and the width-finding algorithm is less likely to find such layers in the residual noise. It is therefore unlikely that the long tails seen in Fig. 4 are due to noise.

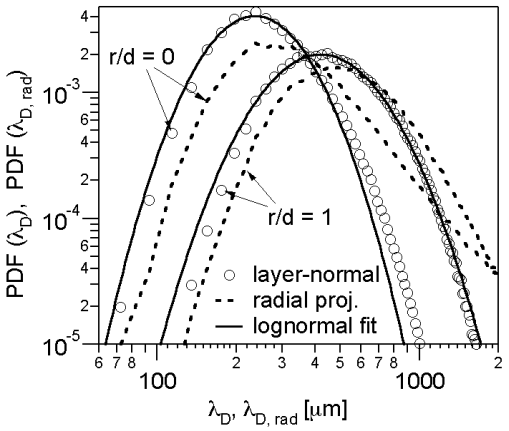

Fig. 5: The same data as in Fig. 4, but on a log-log scale and with log-normal fits to the 2D-width data.

Fig. 5 plots the data of Fig. 4 and the respective log-normal fits to the layer-normal measurements of λ_D on a logarithmic scale. It is seen that the log-normal approximation describes the PDFs reasonably well. The peak of each distribution can therefore be interpreted as its logarithmic mean.

In line measurements and 1-D spectra, like the ones presented above, the local structure is not captured layer-normal, but only in its projection onto the single measurement dimension. For a more accurate comparison, we calculated the radial projection of the layer thicknesses $\lambda_{D,rad} = \lambda_D/|\cos(\beta)|$, where β is the local angle between the gradient vector and the radial direction. The resulting PDFs of $\lambda_{D,rad}$ are shown in Fig. 4 and Fig. 5 as dashed lines. The 1-D measurement has the peak of the PDFs shifted to approximately 280 μm and 480 μm for r/d = 0 and r/d = 1, respectively. The PDFs have significantly longer tails, appearing as nearly straight lines in the log-log plot of Fig. 5. At r/d = 0 the flow is closer to isotropic while at r/d = 1 a preferred orientation of the layers leads to a situation more favorable for a radial measurement (steeper slope at high λ_D). These 1-D

artifacts are similar to those encountered in 1-D measurements of the scalar dissipation PDF, which have been explained by theoretical analysis [23].

It is now interesting to locate the peaks of PDF($\lambda_{D,rad}$) in the respective power spectra of Fig. 3a: Assuming locally Gaussian layer profiles, we correct for the effects of smoothing at the spatial scale of the PDFs' peaks, resulting in estimates for the actual peak locations of $\lambda_{D,rad}{}^{C} = 260\ \mu m$ at $r/d = 0$ and $454\ \mu m$ at $r/d = 1$. Both corrected and uncorrected values for $\lambda_{D,rad}$ correspond to about 0.5% of the maximum PSD in the interlaced and smoothed spectrum, respectively. The length scales found from PDFs and their corresponding PSDs are summarized in Table 1.

	λ_D [μm]	$\lambda_D{}^C$ [μm]	$\lambda_{D,rad}$ [μm]	$\lambda_{D,rad}{}^C$ [μm]
r/d = 0	240	216	280	260
⇔ 1/λ [mm^{-1}]	4.17	4.63	3.57	3.85
fraction of pk. PSD [%]			0.52	0.72
r/d = 1	400	368	480	454
⇔1/λ [mm^{-1}]	2.5	2.72	2.08	2.2
fraction of pk. PSD [%]			0.47	0.54

Table 1: Length scales in 2D and 1D PDFs on the layer thickness. As-measured and estimated corrected values.

These results suggest that the characteristic length scale at this downstream location in the flame could be determined from the spatial frequency corresponding the 0.5%-of-peak interlaced power spectrum. Since the spectra have a very steep slope at these high frequencies, using 1% or 0.25% will result in similar estimates for $\lambda_{D,rad}$. The major source of uncertainty is that the accuracy in calculating the PDF(λ_D) degrades rapidly for small values of λ_D. However, as stated above, the layer widths corresponding to the peaks of the 2D-PDFs are measured accurately to within about 10%.

4 Conclusion

High-resolution two-dimensional temperature measurements were performed in the near field (x/d=10) of a turbulent jet flame. The $|\nabla T'|^2$-field was used to characterize the spatial scales of dissipative structures. Fully resolved power density spectra of the temperature gradients were measured using a novel interlacing technique to suppress noise. This noise-suppression technique is well-suited for imaging measurements that are oversampled in at least one dimension. The instantaneous dissipative structures occurred in layers with a range of thicknesses. The PDFs of the 20%-full-width layer thicknesses had peak values at $216\ \mu m$ and $368\ \mu m$ for $r/d = 0$ and $r/d = 1$, respectively. Uncertainty estimates indicated that these layer thicknesses can be measured with approximately 10% uncertainty using effective spatial resolutions of $41\ \mu m$ and $62\ \mu m$ at $r/d = 0$ and $r/d=1$, respectively. The projection of the layers onto the radial direction indicated that a 1-D measurement increased the length scale of the PDF peak by approximately 20%. The conversion of this length scale to a spatial frequency revealed that the spectral density was approximately 0.5% of its peak value for length scales on the order of the dissipation layer thickness. Ongoing investigations will more extensively examine the relationship between power spectra and directly measured structure thicknesses throughout a larger part of the near field ($5 \le x/d \le 20$) and quantify the allocation of dissipation amongst these layered structures, as has been done for non-reacting flows [25].

Acknowledgments

The authors thank Dr. G. H. Wang for helpful discussions and R. J. Sigurdsson for excellent technical assistance in the laboratory. This research was supported by the U.S. Department of Energy, Office of Basic Energy Sciences, Division of Chemical Sciences, Geosciences, and Biosciences. Sandia National Laboratories is a multiprogram laboratory operated by Sandia Corporation, a Lockheed Martin Company, for the U.S. Department of Energy under contract DE-AC04-94-

AL85000.

References

1. V. Bergmann, W. Meier, D. Wolff, W. Stricker, *Appl. Phys. B* 66 (1998) 489-502.
2. J. Mi, R.A. Antonia, *Exp. Thermal and Fluid Sci.* 8 (1994) 328-335.
3. D. Geyer, *Ph.D. thesis,* Technische Universität Darmstadt (Germany), 2004.
4. A.N. Karpetis, R.S. Barlow, *Proc. Combust. Inst.* 29 (2002) 1929-1936.
5. A.N. Karpetis, R.S. Barlow, *Proc. Combust. Inst.* 30 (2005) 665-672.
6. J.H. Frank, S.A. Kaiser, M.B. Long, *Proc. Combust. Inst.* 29 (2002) 2687-2694.
7. J.H. Frank, S.A. Kaiser, M.B. Long, *Combust. Flame* XX (200X) XXX-XXX (accepted for publication)
8. J. Fielding, A.M. Schaffer, M.B. Long, *Proc. Combust. Inst* 28 (1998) 1007-1014.
9. J.B. Kelman, A.R. Masri, S.H. Stårner, R.W. Bilger, *Proc. Combust. Inst* 25 (1994) 1141-1147.
10. W. Meier, R.S. Barlow, Y.-L. Chen, J.-Y. Chen, *Combust. Flame* 123 (2000) 326-343.
11. R.S. Barlow, J.H. Frank, *Proc. Combust. Inst* 28 (1998) 1087-1095.
12. E.R. Hawkes, R. Sankaran, J. Sutherland, J.H. Chen, *submitted for this Symposium*.
13. D. C. Fourguette, R. M. Zurn, M. B. Long, *Combust. Sci. Tech.* 44 (1986) 307-317.
14. D.A. Everest, J.F. Driscoll, D.J.A. Dahm, D.A. Feikama, *Combust. Flame* 101 (1995) 58-68.
15. G.H. Wang, N.T. Clemens, P.L. Varghese, *Proc. Combust. Inst.* 30 (2005) 691-699.
16. K.A. Buch, W.J.A. Dahm, *J. Fluid. Mech.* 364 (1998) 1-29.
17. L.K. Su, N.T. Clemens, *Exp. Fluids.* 27 (1999) 507-521.
18. L.K. Su, N.T. Clemens, *J. Fluid. Mech.* 488 (2003) 1-29.
19. G.H. Wang, N.T. Clemens, P.L. Varghese, *Appl. Optics* 44 (2005) 6741-6751.
20. www.ca.sandia.gov/TNF (Editor: R.S. Barlow).
21. G.H. Wang, N.T. Clemens, *Exp. Fluids* 37 (2004) 194-205.
22. M.S. Tsurikov, N.T. Clemens, *40th Aerospace Science Meeting* (2002), AIAA paper 2002-164.
23. W.J.A. Dahm, K.A. Buch, *Phys. Fluids A* 1 (1989) 1290-1293.
24. M.W. Renfro, J.P. Gore, G.B. King, N.M. Laurendeau, *AIAA J.* (2000) 1230-1236.
25. J. Mi, G.J. Nathan, *Exp. Fluids* 34 (2003) 687–696.